

Electronic Supplementary Information

**Hydrogen Bond Network Structures of Protonated 2,2,2-
Trifluoroethanol/Ethanol Mixed Clusters Probed by Infrared Spectroscopy
Combined with a Deep-learning Structure Sampling Approach: The Origin of
the Linear Type Network Preference in Protonated Fluoroalcohol Clusters[†]**

Po-Jen Hsu,^{‡1} Atsuya Mizuide,^{‡2} Jer-Lai Kuo^{*1}, and Asuka Fujii^{*2}

¹Institute of Atomic and Molecular Sciences, Academia Sinica, Taipei 10617, Taiwan

²Department of Chemistry, Graduate School of Science, Tohoku University,

Sendai 980-8578, Japan

E-mail: jlkuo@pub.iams.sinica.edu.tw (J.-L.K.), asuka.fujii.c5@tohoku.ac.jp (A.F.).

[‡]□Po-Jen Hsu and Atsuya Mizuide contributed equally to this study.

Contents

- Section I** Basin-hopping structural search and geometry operators.
- Section II** Training samples for NNP models
- Section III** Communications among Gaussian 16, Schnetpack, and basin-hopping workers
- Section IV** Schnetpack NNP training scheme.
- Table S1** Numbers of training data for $\text{H}^+\text{T}_m\text{E}_n\text{-Ar}$ clusters ($m + n = 5$).
- Figure S1** The workflow of the parallelized basin-hopping algorithm with N CPU workers.
- Figure S2** The workflow of the basin-hopping worker.
- Figure S3** The training set 0 for the **NNP0** model.
- Figure S4** Energy correlation between **PM6** samples and their single-point calculations at M06-2X/6-311+G(d,p) level.
- Figure S5** Energy correlation between **PM6** samples and their single-point calculations at M06-2X+D3/6-311+G(d,p) level.
- Figure S6** The selection scheme for the optimization snapshots.
- Figure S7** The patching scheme for the NNP model.
- Figure S8** Energy correlation and the mean absolute error (MAE) between test set 0 from **NNP0** minima and single-point calculations at M06-2X+D3 level.
- Figure S9** Energy correlation and the mean absolute error (MAE) between test set 1 from **NNP1** minima and single-point calculations at M06-2X+D3 level.
- Figure S10** Energy correlation and the mean absolute error (MAE) between test set 2 from **NNP2** minima and single-point calculations at M06-2X+D3 level.
- Figure S11** Energy correlation and the mean absolute error (MAE) between test set 3 from **NNP3** minima and single-point calculations at M06-2X+D3 level.
- Figure S12** Force correlation and the mean absolute error (MAE) between test set 0 from **NNP0** minima and single-point calculations at M06-2X+D3 level.
- Figure S13** Force correlation and the mean absolute error (MAE) between test set 1 from **NNP1** minima and single-point calculations at M06-2X+D3 level.

- Figure S14** Force correlation and the mean absolute error (MAE) between test set 2 from **NNP2** minima and single-point calculations at M06-2X+D3 level.
- Figure S15** Force correlation and the mean absolute error (MAE) between test set 3 from **NNP3** minima and single-point calculations at M06-2X+D3 level.
- Figure S16** The histogram of errors for energies on test set 0.
- Figure S17** The histogram of errors for energies on test set 1.
- Figure S18** The histogram of errors for energies on test set 2.
- Figure S19** The histogram of errors for energies on test set 3.
- Figure S20** The histogram of zero-point corrected energies at M06-2X+D3 level for **NNP0** and **PM6** samples.
- Figure S21** The histogram of zero-point corrected energies at M06-2X+D3 level for **NNP1** and **PM6+NNP0** samples.
- Figure S22** The histogram of zero-point corrected energies at M06-2X+D3 level for **NNP2** and **PM6+NNP0+NNP1** samples.
- Figure S23** The histogram of zero-point corrected energies at M06-2X+D3 level for **NNP3** and **PM6+NNP0+NNP1+NNP2** samples.
- Figure S24** Comparison between the experimental and simulated IR spectra from the **PM6** and replacement samples.
- Figure S25** Comparison between the experimental and simulated IR spectra from **NNP0**, **PM6**, and replacement samples.
- Figure S26** Comparison between the experimental and simulated IR spectra from **NNP0**, **NNP1**, **PM6**, and replacement samples.
- Figure S27** Comparison between the experimental and simulated IR spectra from **NNP0**, **NNP1**, **NNP2**, **PM6**, and replacement samples.
- Figure S28** Energy correlation and the mean absolute error (MAE) between test set 3 from **NNP3** minima and their geometry optimization at M06-2X+D3 level.
- Figure S29** Comparison of optimization steps in DFT.
- Figure S30** Statistics of shape similarity between **NNP3** minima and the corresponding DFT minima.

I. Basin-hopping structural search and geometry operators

A basin-hopping searching process contains multiple steps to manipulate the cluster structure. We designed four geometry operators for this purpose (Fig. S2):

a. Drag and release operator:

For a randomly selected molecule, a distant point along any direction from the molecule's center of mass (COM) is chosen as a release point. The molecule is then pulled back from that point along the opposite direction and released towards the optimal position within the original molecular system, bringing the moving molecule closer to other molecules. To prevent atoms from getting too close, the distance between atoms of different molecules must be greater than 1.2 times the sum of their Van der Waals radii.

b. Random move operator:

Each molecule undergoes random translations and rotations, with movements less than 2 angstroms and rotations less than 60 degrees.

c. Shuffle operator:

We adopted an algorithm previously used for random search.¹ Molecules are randomly distributed and rotated within an 8x8x8 (in angstrom) cell. The distance between each pair of molecules must be larger than 5 and smaller than 9 angstroms simultaneously.

d. Bond rotation operator:

Specifically designed for ethanol and trifluoroethanol, this operator randomly rotates all the C-C and C-O bonds within a given rotation range.

We can adjust the probabilities of selecting these four operators at each step. For example, we found the Drag-and-Release operator to be highly effective in finding new H-bonded structures. Therefore, we set its probability to 50%. The probabilities for Random Move and Shuffle are each set to 10%. We also employed three types of Bond rotation operators, with rotation angles ranging from [-30, 30], [-60, 60], and [-120, 120] degrees, simulating small to large-scale bond rotations. Each bond rotation operator has a probability of 10% of being executed.

In each basin-hopping step, one of these operators is chosen based on the abovementioned probabilities to find the new cluster structure. The newly found

structure will undergo geometry optimization. The acceptance of the optimized structure is checked based on two criteria:

1. It is rejected if the structure is unreasonable, such as having a broken covalent bond.
2. Given a random number between 0 and 1, if it is smaller than $e^{-(E_{\text{new}}-E_{\text{old}})/kT}$, the structure is accepted and replaces the old one.

Since we are not searching only for the global minimum, all the accepted structures are retained in a database.

II. Training samples for NNP models

Our NNP training is divided into an initial model (NNP0) and patched model (NNP1, NNP2, etc.) trainings. The corresponding training samples are listed in Table S1 and described below:

1. Replacement samples:

We started with the H^+T_3 structures with Ar from Ref. 1, selecting 14 linear and 24 cyclic structures, which are structures with probabilities greater than 0.1 in Q-HSA calculations below 200K. We replaced the CF_3 group with a CH_3 group, considering all possible substitutions to generate $\text{H}^+\text{T}_m\text{E}_n\text{-Ar}$ clusters. These structures were optimized, and frequency calculations were conducted using M06-2X/6-311+G(d, p) (with or without GD3 correction) (Fig. S3). In the preliminary analysis of the stability of linear and cyclic H-bonded species, we found that the dispersion effect greatly influenced ethanol-rich ($n > 2$) clusters, changing the representative H-bonded structures. Conversely, the correction had less impact on TFE-rich clusters ($n < 3$). Moreover, our previous study shows that for the H^+E_4 cluster, the dispersion correction cannot be ignored.² While M06-2X already includes mid-range electronic correction, the dispersion correction supplements long-range interactions. We employed Grimme's GD3 correction with a damped R^{-6} term correction ($\text{SR6} = 1.619$), included in the Gaussian 16 software.³ We will refer to the corrected level of theory as M06-2X+D3 in the following paragraphs.

2. PM6 samples:

Since direct structural search using DFT is time and resource-consuming, we previously used DFTB3 or random search to obtain structural samples, which were then optimized with DFT. We conducted basin-hopping structural searches using the PM6 method instead of DFTB3 to complement replacement samples because the DFTB3 library (3ob-3-1) we used did not provide parameters for Ar.⁴⁻⁷ After obtaining the search samples, we re-optimized them using M06-2X(+D3). We found a poor correlation between PM6 and M06-2X, with mean absolute errors (MAE) of energies exceeding 50 kJ/mol (Fig. S4 and S5). Since the PM6 samples are not entirely unreasonable (e.g., large intermolecular distances), they can provide suitable initial samples and offer sufficient force and energy training data during the M06-2X optimization process. While methods such as PM7 or DFTB3 may provide results closer to DFT, we aimed to exclude the impact of a particular semi-empirical potential on the NNP training. With a preliminary usable NNP model, we replaced semi-

empirical methods with NNP for structural searches and iteratively refined this model. For simplicity, we use the label **PM6** to indicate the DFT-optimized structures of PM6 and replacement samples.

3. **NNP0 samples:**

We combined the GD3-corrected minima from II.1 and II.2 and used an exponential function to extract optimization snapshots (20 for each minimum, see Fig. S6). These snapshots provide forces and energies as the training set 0 for the **NNP0** model training. Basin-hopping structural searches were performed using **NNP0** to obtain the distinct minima as test set 0 (Fig. S7(a)). The mean absolute error was evaluated by comparing NNP energies with their M06-2X+D3 single-point energies. The patch set 0 was extracted from the test set 0 in which the errors of the data points exceeded 3 kJ/mol.

4. **Iterative patching samples from the NNP structure searches:**

Patch set 0 was added to training set 0 to build training set 1. Using **NNP0** as a basis and the training set 1, the **NNP1** model was generated (Fig. S7(b)), and basin-hopping structural searches were conducted with the **NNP1** model to establish test set 1. Again, test set 1 was evaluated using M06-2X+D3 single-point calculations to assess the MAE of energies. Those with errors larger than 3 kJ/mol will be retained as the new patching data (Fig. S7(c)). We utilized the same iterative procedure to generate the new models (e.g., **NNP2** and **NNP3**).

III. **Communications among Gaussian 16, Schnetpack, and basin-hopping workers**

To integrate Gaussian optimization tasks with Neural Network Potential (NNP) predictions, we developed interfaces linking Gaussian, Schnetpack, and our basin-hopping code (Fig. S2). At each step, the basin-hopping code generates the necessary Gaussian input file and performs the optimization job, yielding optimized coordinates, forces, and energy. This approach enables the use of the PM6 semi-empirical potential, Density Functional Theory (DFT) level of theory, and Schnetpack models in conjunction with Gaussian's built-in Berny optimization algorithm.⁸ For geometry optimization using a Schnetpack NNP model, an external Python code is employed to predict forces and energy with given coordinates during the process. The route section of the Gaussian input file used for this external code is shown in Fig. S2 (i.e.,

external="\$NNP_predictor.py NNP_model" where \$NNP_predictor.py refers to an actual Python script). Finally, the Message Passing Interface (MPI) protocol is used to distribute the optimization tasks of each basin-hopping worker across the computational resources (Fig. S1).

IV. Schnetpack NNP training scheme

We used the Schnetpack deep-learning package for training the NNP model, employing 4 interaction layers, 75 sets of radial functions for describing the interatomic distances, and 128 sets of features in the output layer to describe atomic interactions and energies.⁹ As for the loss function, we include the energy (E) and the interatomic forces (F) as follows:

$$\mathcal{L}(E_{\text{ref}}, \mathbf{F}_{\text{ref}}, E_{\text{pred}}, \mathbf{F}_{\text{pred}}) = \frac{1}{n_{\text{train}}} \sum_{n=1}^{n_{\text{train}}} \left[\rho_1 (E_{\text{ref}} - E_{\text{pred}})^2 + \frac{\rho_2}{3N_{\text{atoms}}} \sum_{\alpha}^{N_{\text{atoms}}} \|\mathbf{F}_{\text{ref}}^{(\alpha)} - \mathbf{F}_{\text{pred}}^{(\alpha)}\|^2 \right]$$

where *ref* and *pred* stand for referenced and predicted data, respectively, and the force difference is evaluated by the Euclidean norm. In this loss function, we use the coefficients ρ_1 and ρ_2 to determine the contributions of energy and forces. After several attempts, the best training result was obtained with $\rho_1 = 0.01$ and $\rho_2 = 1 - \rho_1$, which can reduce the mean absolute error (MAE) of energy and forces to less than 2 kJ/mol. In each training session, we used 32 batches to maintain a reasonable GPU memory usage. The training facility we used was a single Nvidia Tesla V100 GPU with 32GB memory (Taiwania 2 cluster) at National Center for High-performance Computing in Taiwan.

To ensure training convergence, we employed the Warm-restart learning rate scheduler. Additionally, we conducted 5 training sessions, with initial learning rates ranging from 0.001 to 0.0005. During the training, 10% of the training set will be chosen as the validation set. After each training finishes, we select the model with the lowest validation loss and MAE on the validation set.

The correlation between the NNP predictions and DFT single-point calculations and the mean absolute error of energies (EMAE) and forces (FMAE) of **NNP0**, **NNP1**, **NNP2**, and **NNP3** are presented in Fig. S8 – S15. We further analyze the distribution of the energy errors to resolve the dense data points in the energy correlations (Fig. S16 – S19). The EMAE and FMAE are improved from **NNP0** to **NNP2**. The DFT minima derived from the **NNP2** minima almost cover the low-energy range of the previous DFT results (Fig. S20 – S22). Therefore, we considered the subsequent models converged and used the **NNP3** model patched from **NNP2** for the production run. More than 15 basin-hopping searching cycles were conducted extensively to search test set 3 with the **NNP3** model. Due to the large size of test set 3, the EMAE slightly increased from test set 2. Nevertheless, the **NNP3** model is sufficiently

accurate overall, with an average EMAE of around 1.819 kJ/mol.

	H ⁺ E ₅ -Ar	H ⁺ T ₁ E ₄ -Ar	H ⁺ T ₂ E ₃ -Ar	H ⁺ T ₃ E ₂ -Ar	H ⁺ T ₄ E ₁ -Ar	H ⁺ T ₅ -Ar
Training set 0 (PM6, NNP0)	7,695	7,862	4,558	4,356	4,290	1,112
Patch set 1 (NNP1)	260	352	352	587	421	379
Patch set 2 (NNP2)	173	123	135	169	134	128
Patch set 3 (NNP3)	132	204	114	181	175	104

Table S1. Numbers of training data for H⁺T_{*m*}E_{*n*}-Ar clusters ($m + n = 5$). The training set 0 includes the snapshots obtained from the geometry optimization at M06-2X+D3/6-311+G(d,p) level from the **PM6** samples. The patch sets were obtained from the single-point calculations at the same DFT level. The training set was expanded with the patch set to generate the new NNP model. For example, the training set 3 for **NNP3** model includes training set 0, patch set 1, patch set 2, and patch set 3.

Parallelized Basin-Hopping scheme

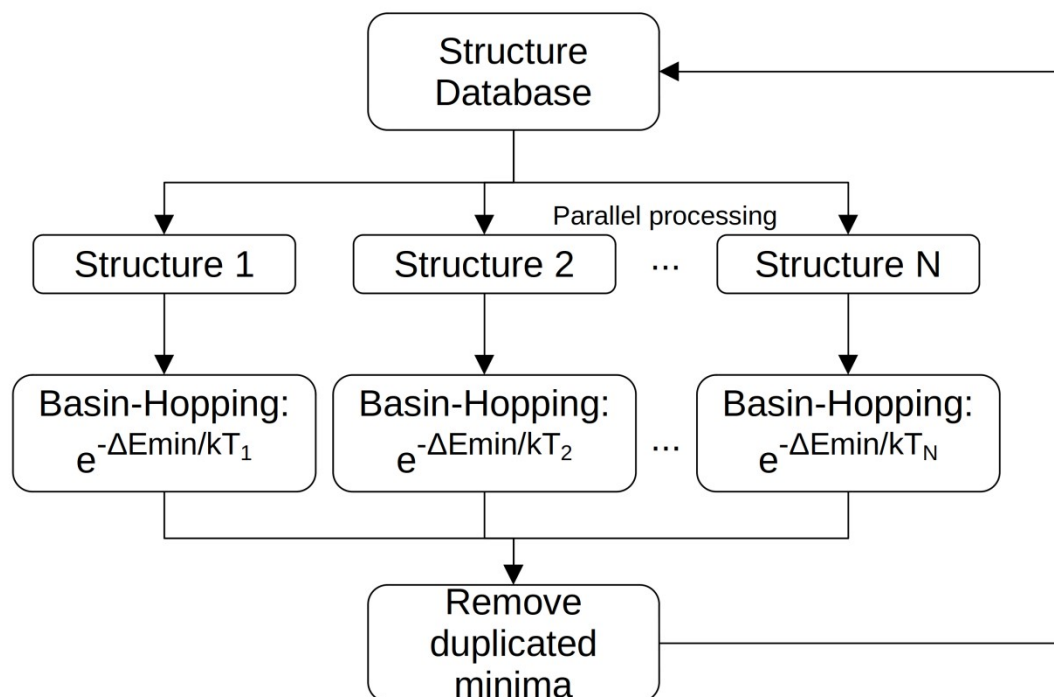


Figure S1. The workflow of the parallelized basin-hopping algorithm with N CPU workers. Each worker selects an initial structure from a structure database and has its T parameter for the transition probability of the newly searched local minimum in this work. When a series of basin-hopping steps finishes (100 steps), all accepted local minima are collected, duplicates are removed, and the structure database is updated. The next cycle will randomly select initial structures from the updated structure database based on Boltzmann weight for a new basin-hopping search. In this work, this process is repeated for at least two cycles or more. The T parameters are evenly chosen from 200 to 2000 for 24 CPU workers.

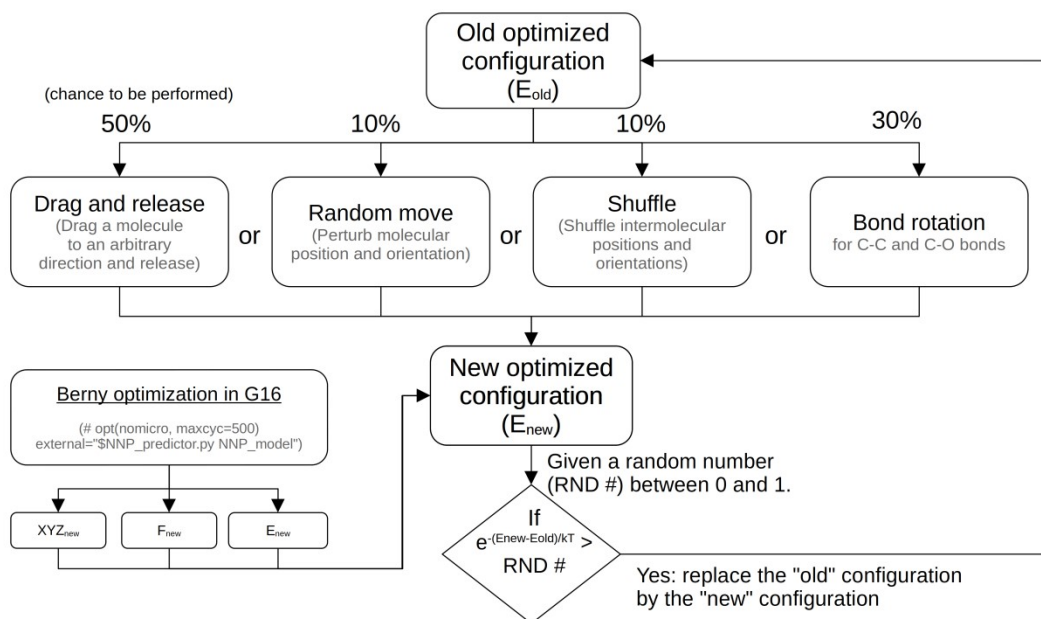


Figure S2. The workflow of the basin-hopping worker. One of four geometric operators is applied to the current configuration, with the choice of operator determined by its selection probability. The resulting configuration is then optimized using a potential model, either the Neural Network Potential (NNP) or the semi-empirical PM6 method, implemented through the Benny algorithm in Gaussian 2016 (G16) software.⁸ A random number, uniformly distributed between 0 and 1, is generated to assess the transition probability. If this number is lower than the predefined transition probability, the new configuration is accepted and replaces the previous one. If not, the new configuration is discarded, and the original configuration is retained for subsequent iterations.

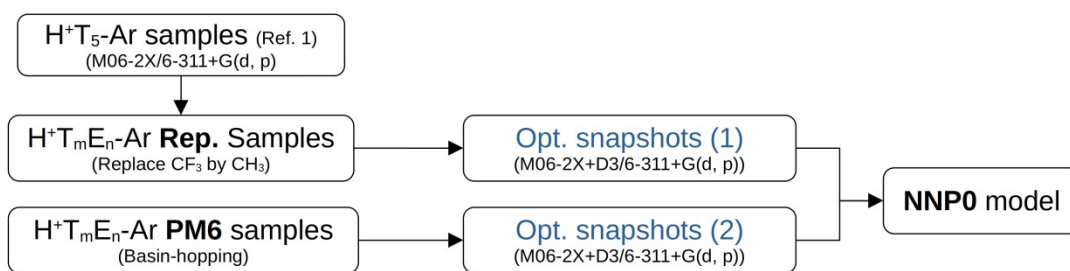


Figure S3. The training set 0 for the **NNPO** model. We used the H^+T_5 samples from ref. 1 to create structures for $H^+T_mE_n$ -Ar ($m + n = 5$) by replacing CF_3 with CH_3 groups and considering all possible combinations for m trifluoroethanol and n ethanol molecules. Additionally, we performed basin-hopping structure searches with the PM6 method. Finally, we combined data from both approaches and optimized them using M06-2X+D3/6-311+G(d,p). The optimization snapshots were extracted to obtain training set 0.

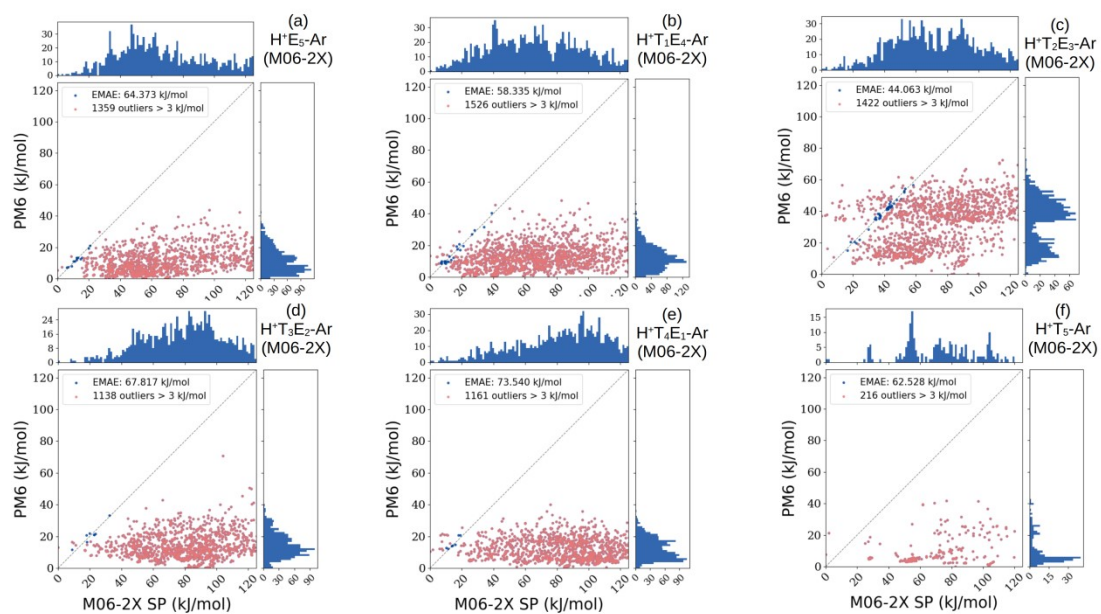


Figure S4. Energy correlation between **PM6** samples and their single-point calculations at M06-2X/6-311+G(d,p) level for (a) H⁺E₅-Ar, (b) H⁺T₁E₄-Ar, (c) H⁺T₂E₃-Ar, (d) H⁺T₃E₂-Ar, (e) H⁺T₄E₁-Ar, and (f) H⁺T₅-Ar.

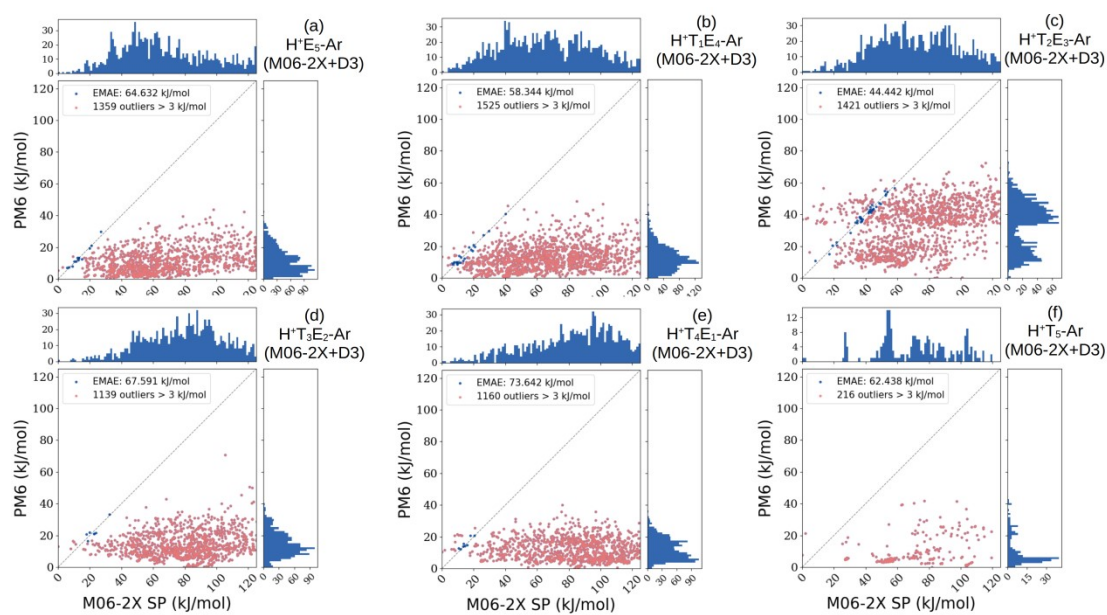


Figure S5. Energy correlation between **PM6** samples and their single-point calculations at M06-2X+D3/6-311+G(d,p) level for (a) $\text{H}^+\text{E}_5\text{-Ar}$, (b) $\text{H}^+\text{T}_1\text{E}_4\text{-Ar}$, (c) $\text{H}^+\text{T}_2\text{E}_3\text{-Ar}$, (d) $\text{H}^+\text{T}_3\text{E}_2\text{-Ar}$, (e) $\text{H}^+\text{T}_4\text{E}_1\text{-Ar}$, and (f) $\text{H}^+\text{T}_5\text{-Ar}$.

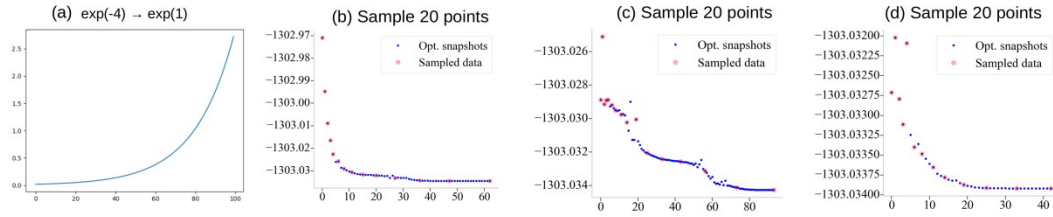


Figure S6. The selection scheme for the optimization snapshots. We uniformly sample 20 points between e^{-4} and e^1 as the ratio of sampling intervals (a). These ratios are then applied to the optimization trajectory to obtain the sampled data points (b - d). In the early stages of optimization, where energy decreases rapidly, there are more sampled points (smaller intervals). As optimization progresses and energy changes slow down towards the end, the number of sampled points decreases (larger intervals).

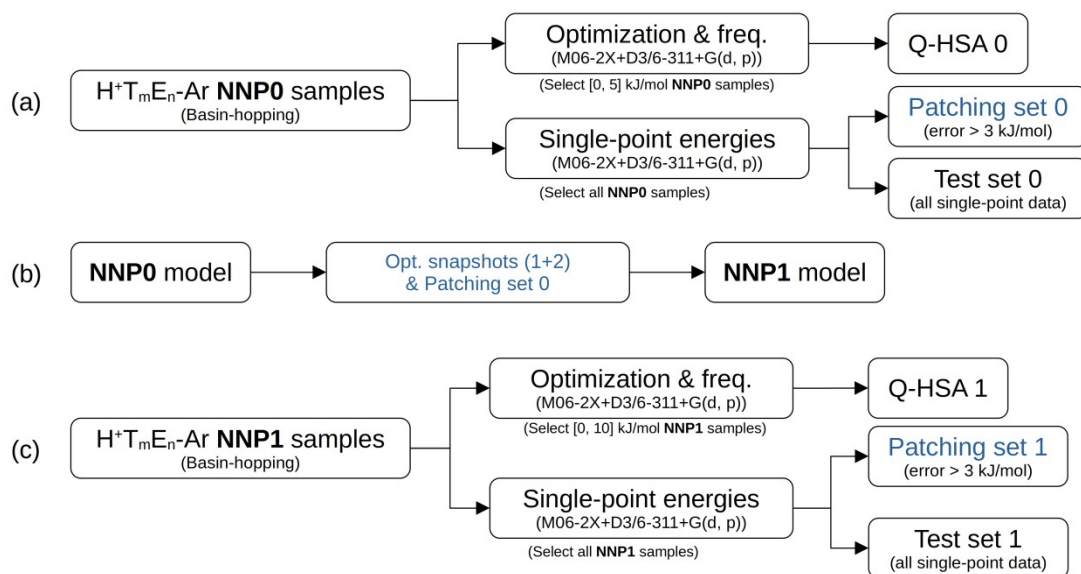


Figure S7. The patching scheme for the NNP model. (a) Starting from an existing NNP model (e.g., NNPO), we performed basin-hopping structure searches to obtain a structure database of distinct minima. Then, we applied M06-2X+D3 single-point calculations to the database to form test set 0 and analyzed the mean absolute error in energy and forces. Data points with errors greater than 3 kJ/mol were classified as patch set 0. Additionally, we re-optimized low-energy structures using M06-2X+D3 and performed frequency calculations for Q-HSA and IR spectra analysis (Q-HSA 0). (b) Finally, patch set 0 is added to the training set 0 to update NNPO to the NNPI model. (c) The new NNPI model can be used to generate test set 1 and patch set 1 and to reassess the IR spectra (Q-HSA 1). Same procedure to generate NNPI2, NNPI3, and so on.

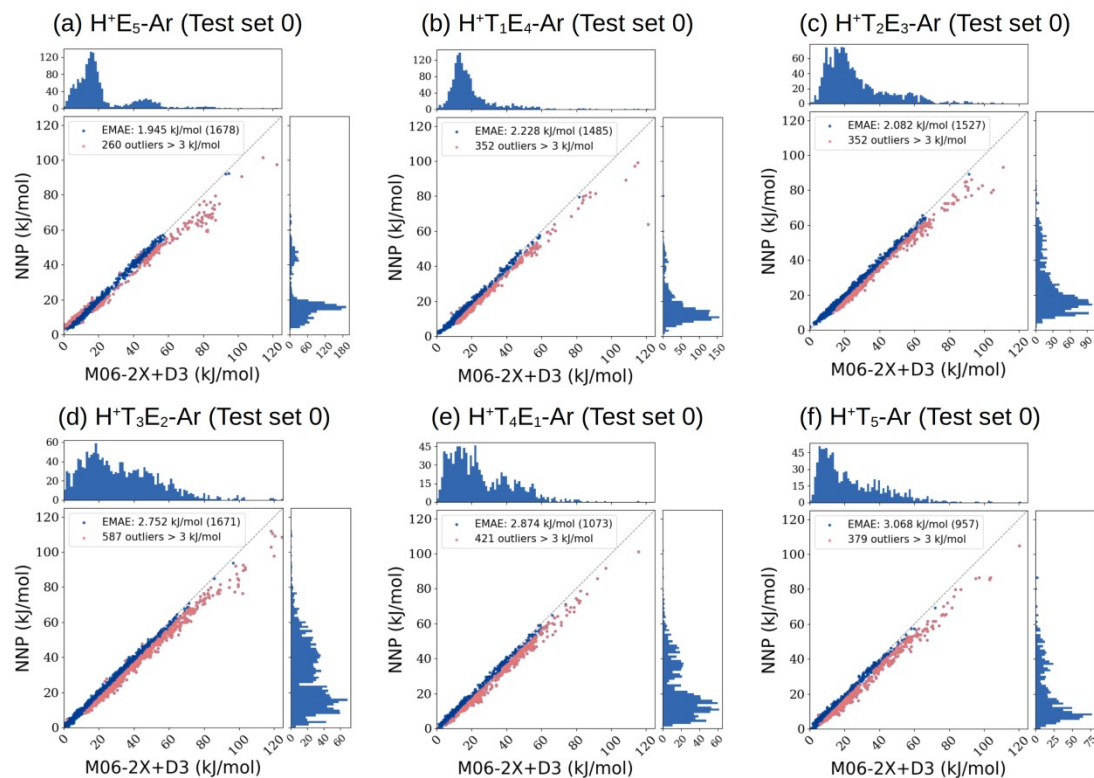


Figure S8. The energy correlation and mean absolute error (MAE) between test set 0, derived from **NNP0** minima, and single-point calculations conducted at the M06-2X+D3 level for the systems (a) H^+E_5 -Ar, (b) $H^+T_1E_4$ -Ar, (c) $H^+T_2E_3$ -Ar, (d) $H^+T_3E_2$ -Ar, (e) $H^+T_4E_1$ -Ar, and (f) H^+T_5 -Ar. The global minimum obtained from the M06-2X+D3 calculations serves as the reference zero energy. Data points with deviations greater than 3 kJ/mol (outliers) are highlighted in red. The sizes of the test sets and the corresponding number of outliers are provided in the accompanying legend.

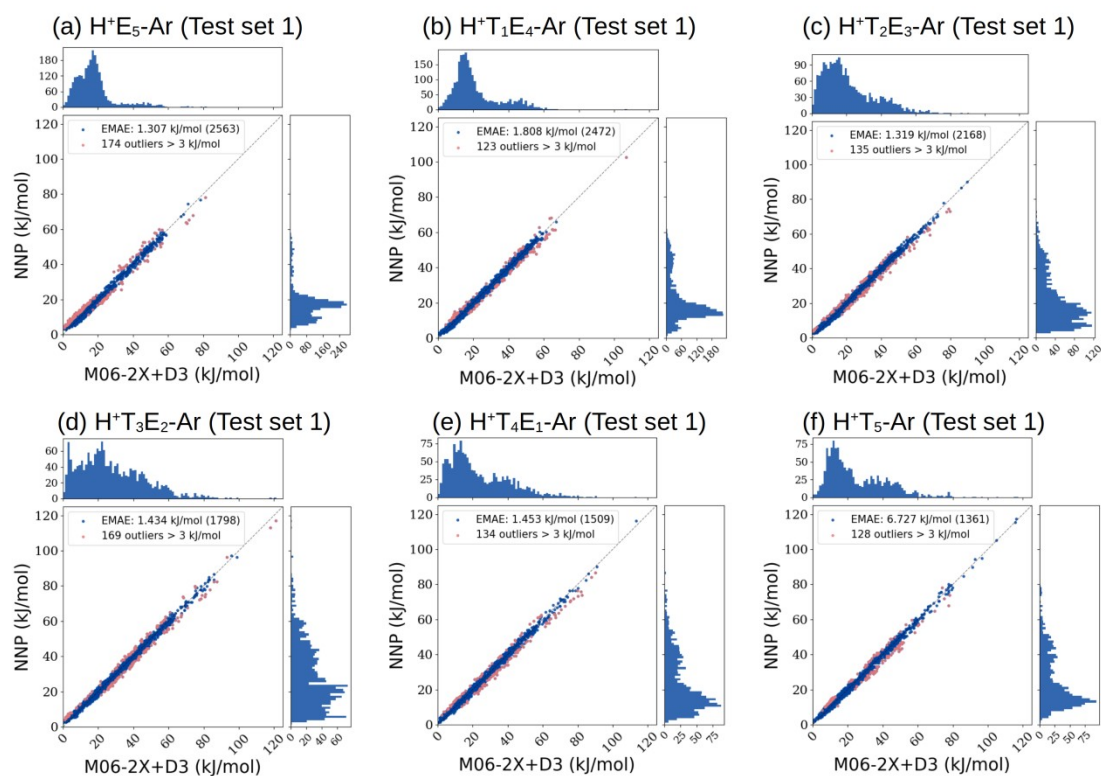


Figure S9. The energy correlation and mean absolute error (MAE) between test set 1, derived from NNP1 minima, and single-point calculations conducted at the M06-2X+D3 level for the systems (a) H^+E_5 -Ar, (b) $H^+T_1E_4$ -Ar, (c) $H^+T_2E_3$ -Ar, (d) $H^+T_3E_2$ -Ar, (e) $H^+T_4E_1$ -Ar, and (f) H^+T_5 -Ar. The global minimum obtained from the M06-2X+D3 calculations serves as the reference zero energy. Data points with deviations greater than 3 kJ/mol (outliers) are highlighted in red. The sizes of the test sets and the corresponding number of outliers are provided in the accompanying legend.

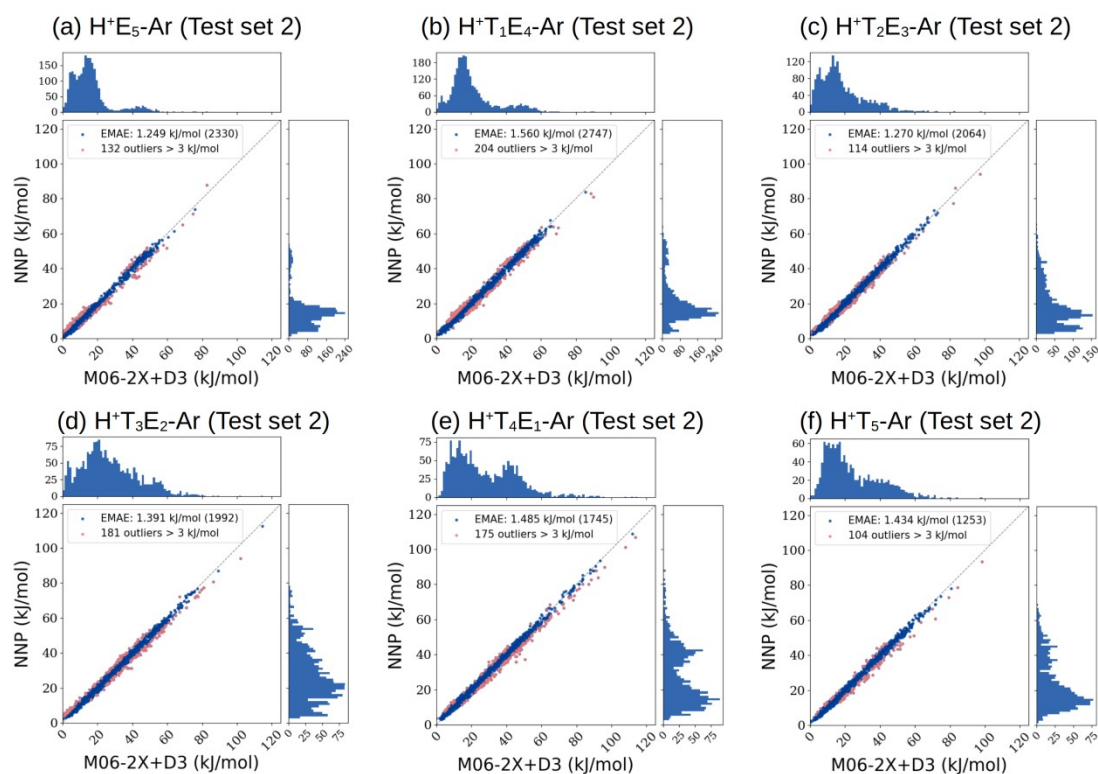


Figure S10. The energy correlation and mean absolute error (MAE) between test set 2, derived from **NNP2** minima, and single-point calculations conducted at the M06-2X+D3 level for the systems (a) H^+E_5 -Ar, (b) $H^+T_1E_4$ -Ar, (c) $H^+T_2E_3$ -Ar, (d) $H^+T_3E_2$ -Ar, (e) $H^+T_4E_1$ -Ar, and (f) H^+T_5 -Ar. The global minimum obtained from the M06-2X+D3 calculations serves as the reference zero energy. Data points with deviations greater than 3 kJ/mol (outliers) are highlighted in red. The sizes of the test sets and the corresponding number of outliers are provided in the accompanying legend.

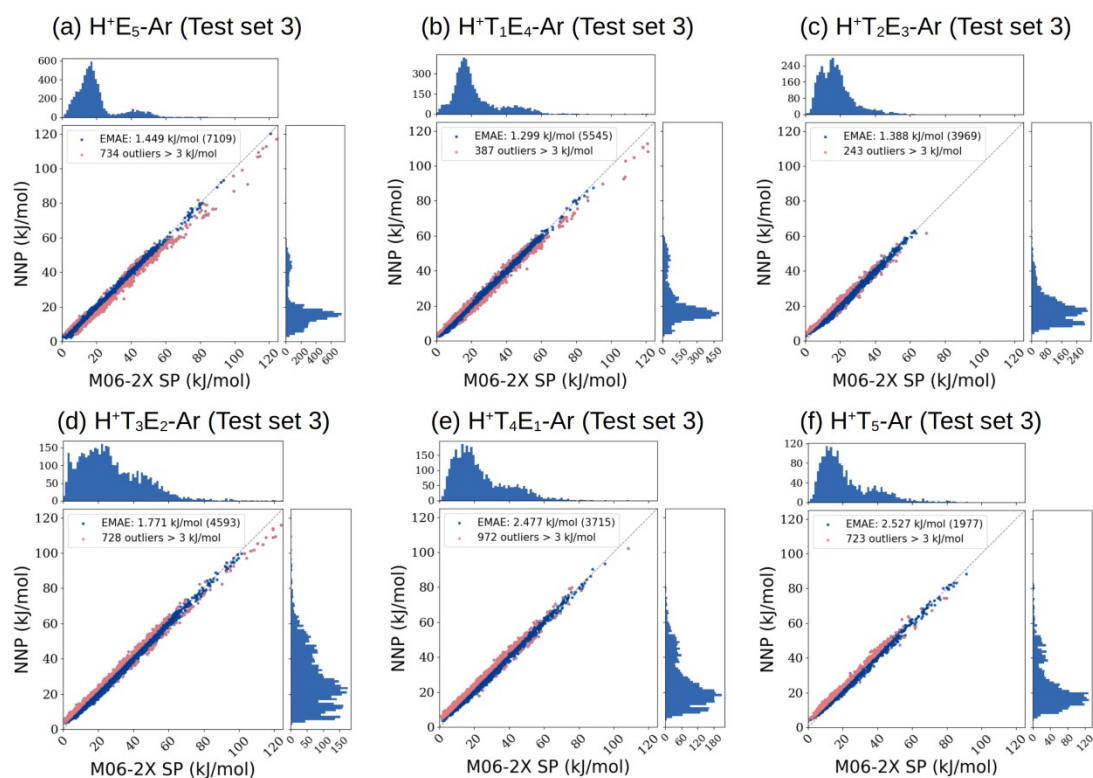


Figure S11. The energy correlation and mean absolute error (MAE) between test set 3, derived from **NNP3** minima, and single-point calculations conducted at the M06-2X+D3 level for the systems (a) H^+E_5 -Ar, (b) $H^+T_1E_4$ -Ar, (c) $H^+T_2E_3$ -Ar, (d) $H^+T_3E_2$ -Ar, (e) $H^+T_4E_1$ -Ar, and (f) H^+T_5 -Ar. The global minimum obtained from the M06-2X+D3 calculations serves as the reference zero energy. Data points with deviations greater than 3 kJ/mol (outliers) are highlighted in red. The sizes of the test sets and the corresponding number of outliers are provided in the accompanying legend.

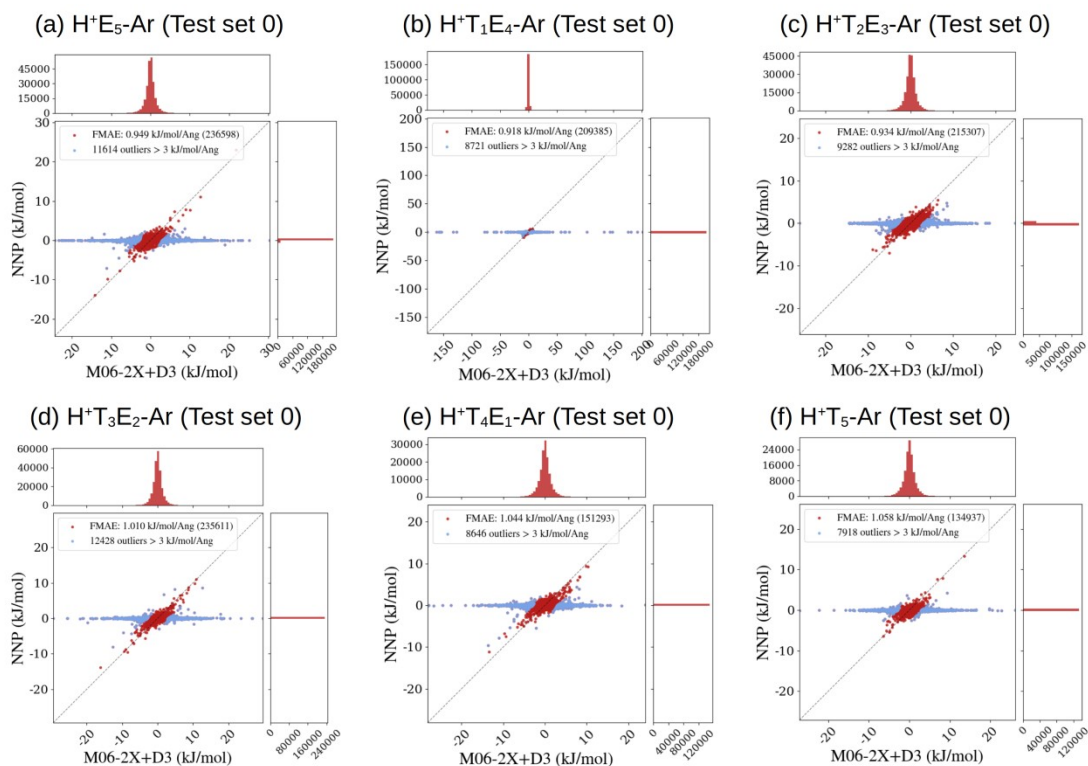


Figure S12. The force correlation and mean absolute error (MAE) between test set 0, derived from **NNP0** minima, and single-point calculations performed at the M06-2X+D3 level for the systems (a) H^+E_5 -Ar, (b) $H^+T_1E_4$ -Ar, (c) $H^+T_2E_3$ -Ar, (d) $H^+T_3E_2$ -Ar, (e) $H^+T_4E_1$ -Ar, and (f) H^+T_5 -Ar. Data points with deviations exceeding 3 kJ/mol·Å (outliers) are marked in blue. The test set sizes and corresponding number of outliers are detailed in the accompanying legend.

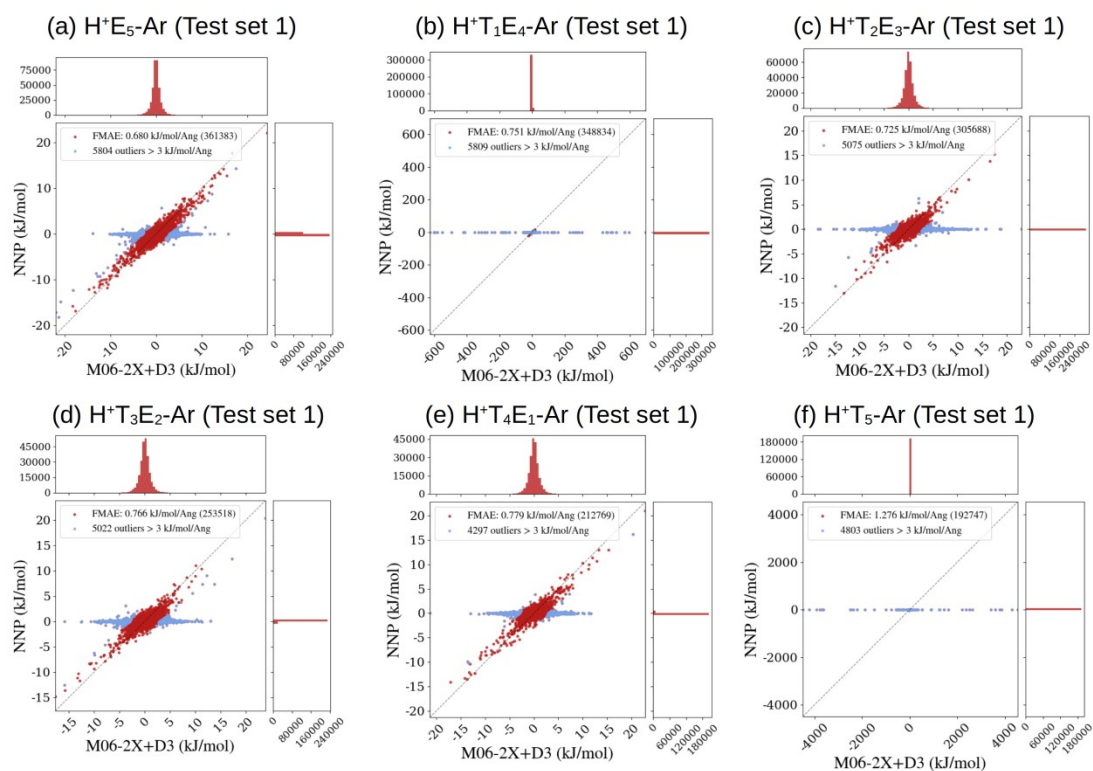


Figure S13. The force correlation and mean absolute error (MAE) between test set 1, derived from NNP1 minima, and single-point calculations performed at the M06-2X+D3 level for the systems (a) H⁺E₅-Ar, (b) H⁺T₁E₄-Ar, (c) H⁺T₂E₃-Ar, (d) H⁺T₃E₂-Ar, (e) H⁺T₄E₁-Ar, and (f) H⁺T₅-Ar. Data points with deviations exceeding 3 kJ/mol·Å (outliers) are marked in blue. The test set sizes and corresponding number of outliers are detailed in the accompanying legend.

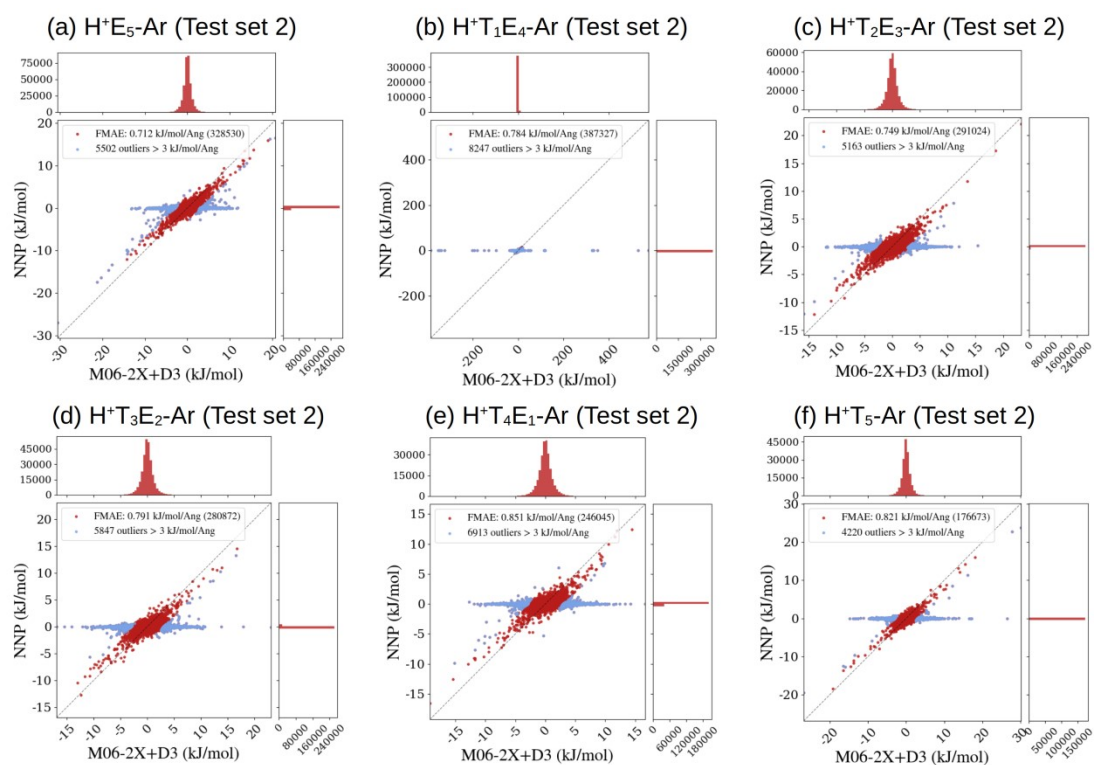


Figure S14. The force correlation and mean absolute error (MAE) between test set 2, derived from NNP2 minima, and single-point calculations performed at the M06-2X+D3 level for the systems (a) H^+E_5 -Ar, (b) $H^+T_1E_4$ -Ar, (c) $H^+T_2E_3$ -Ar, (d) $H^+T_3E_2$ -Ar, (e) $H^+T_4E_1$ -Ar, and (f) H^+T_5 -Ar. Data points with deviations exceeding 3 kJ/mol·Å (outliers) are marked in blue. The test set sizes and corresponding number of outliers are detailed in the accompanying legend.

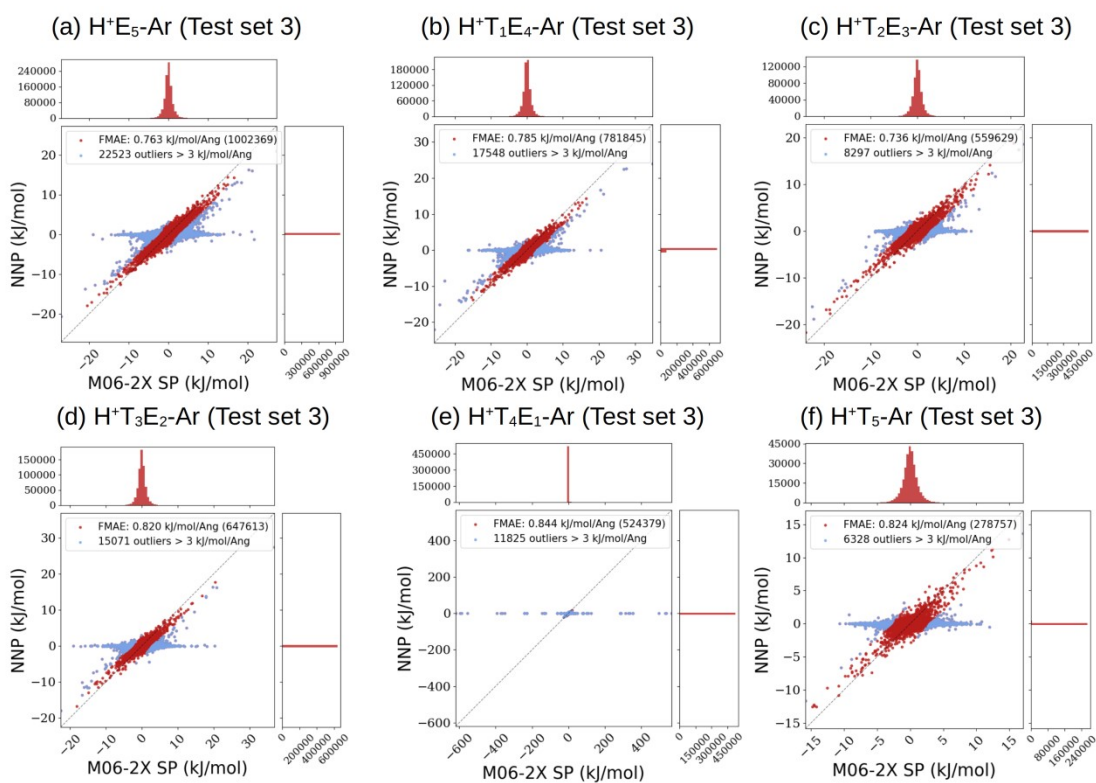


Figure S15. The force correlation and mean absolute error (MAE) between test set 3, derived from NNP3 minima, and single-point calculations performed at the M06-2X+D3 level for the systems (a) H^+E_5 -Ar, (b) $H^+T_1E_4$ -Ar, (c) $H^+T_2E_3$ -Ar, (d) $H^+T_3E_2$ -Ar, (e) $H^+T_4E_1$ -Ar, and (f) H^+T_5 -Ar. Data points with deviations exceeding 3 kJ/mol·Å (outliers) are marked in blue. The test set sizes and corresponding number of outliers are detailed in the accompanying legend.

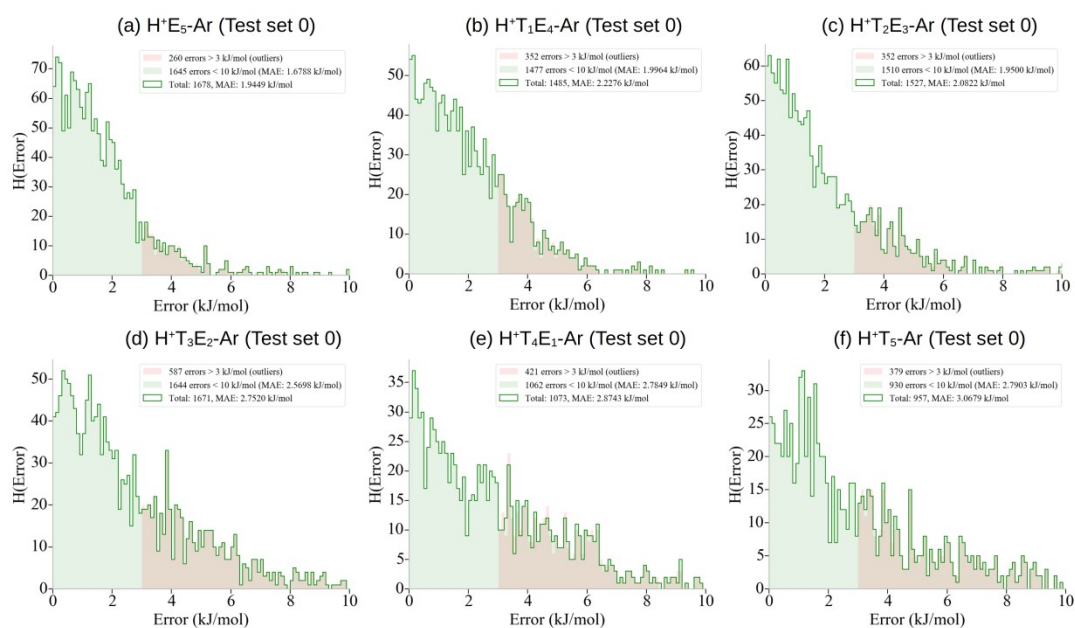


Figure S16. The histogram of energy errors for test set 0 of the systems (a) H^+E_5 -Ar, (b) $H^+T_1E_4$ -Ar, (c) $H^+T_2E_3$ -Ar, (d) $H^+T_3E_2$ -Ar, (e) $H^+T_4E_1$ -Ar, and (f) H^+T_5 -Ar. Data points exhibiting errors exceeding 3 kJ/mol are highlighted in pink. The mean absolute error (MAE) for data points with errors below 10 kJ/mol is provided in the accompanying legend.

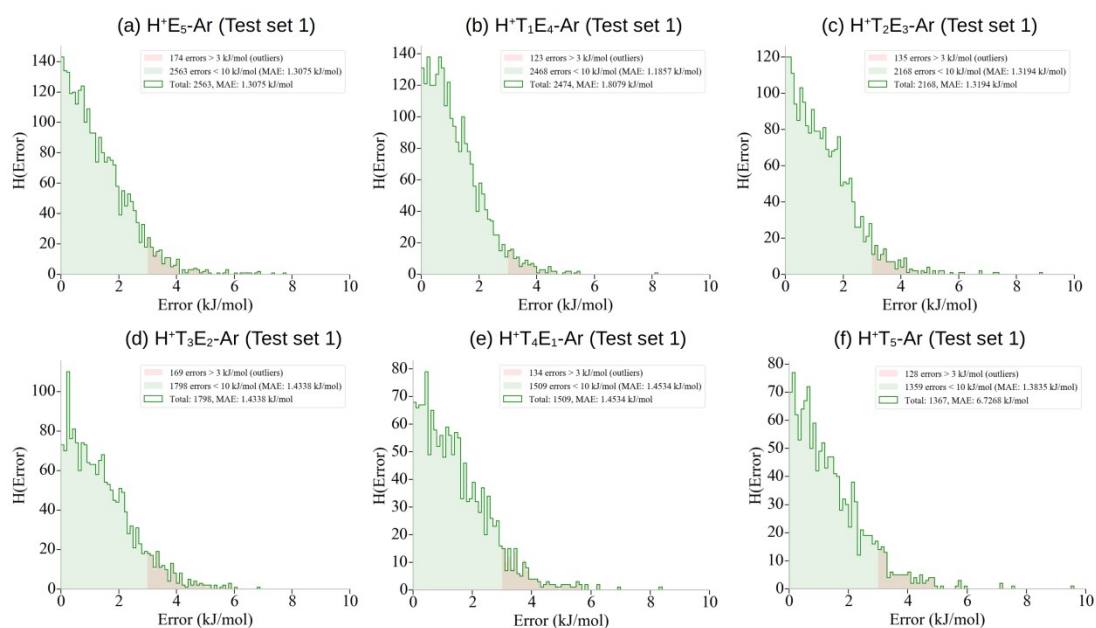


Figure S17. The histogram of energy errors for test set 1 of the systems (a) $H^+E_5\text{-Ar}$, (b) $H^+T_1E_4\text{-Ar}$, (c) $H^+T_2E_3\text{-Ar}$, (d) $H^+T_3E_2\text{-Ar}$, (e) $H^+T_4E_1\text{-Ar}$, and (f) $H^+T_5\text{-Ar}$. Data points exhibiting errors exceeding 3 kJ/mol are highlighted in pink. The mean absolute error (MAE) for data points with errors below 10 kJ/mol is provided in the accompanying legend.

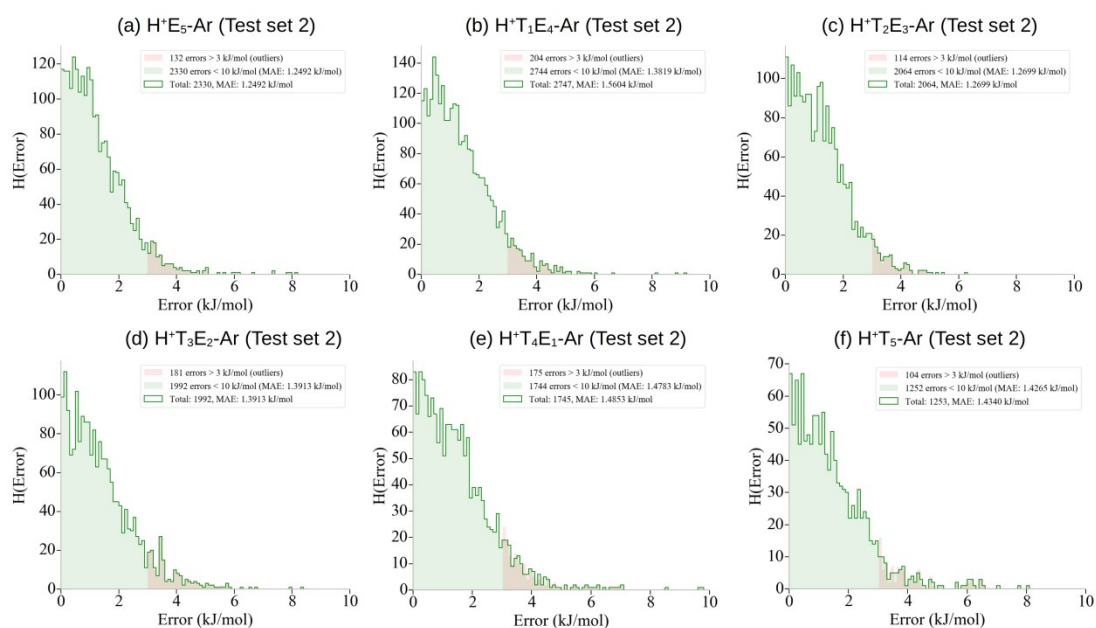


Figure S18. The histogram of energy errors for test set 2 of the systems (a) $H^+E_5\text{-Ar}$, (b) $H^+T_1E_4\text{-Ar}$, (c) $H^+T_2E_3\text{-Ar}$, (d) $H^+T_3E_2\text{-Ar}$, (e) $H^+T_4E_1\text{-Ar}$, and (f) $H^+T_5\text{-Ar}$. Data points exhibiting errors exceeding 3 kJ/mol are highlighted in pink. The mean absolute error (MAE) for data points with errors below 10 kJ/mol is provided in the accompanying legend.

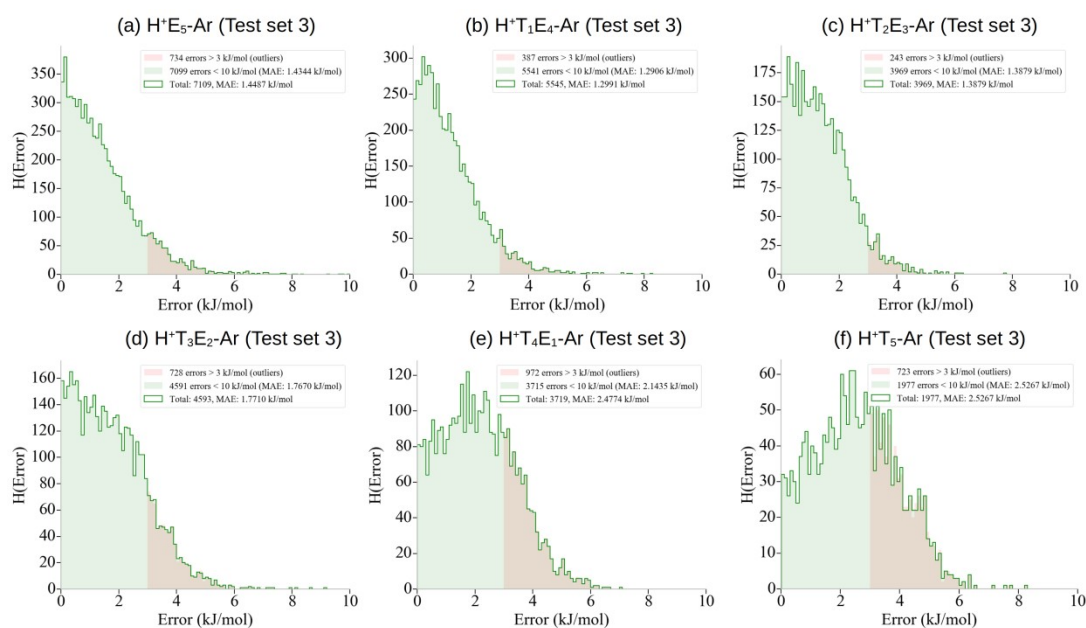


Figure S19. The histogram of energy errors for test set 3 of the systems (a) $H^+E_5\text{-Ar}$, (b) $H^+T_1E_4\text{-Ar}$, (c) $H^+T_2E_3\text{-Ar}$, (d) $H^+T_3E_2\text{-Ar}$, (e) $H^+T_4E_1\text{-Ar}$, and (f) $H^+T_5\text{-Ar}$. Data points exhibiting errors exceeding 3 kJ/mol are highlighted in pink. The mean absolute error (MAE) for data points with errors below 10 kJ/mol is provided in the accompanying legend.

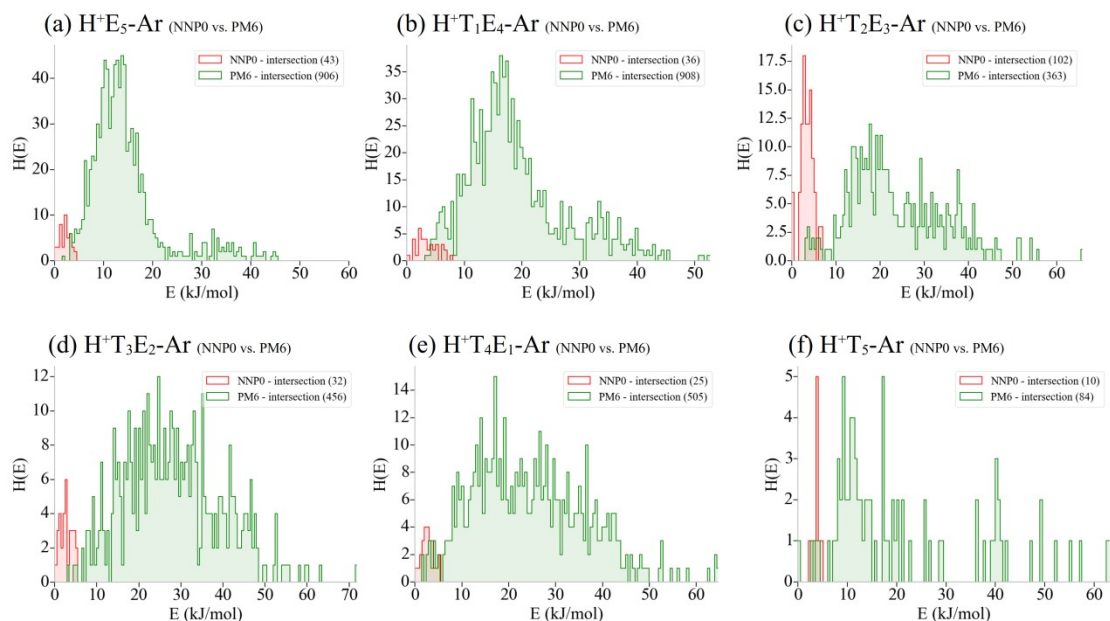


Figure S20. The histogram of zero-point corrected energies for **NNP0** and **PM6** samples. We compared the locally optimized energies at the M06-2X+D3 level from **NNP0** (test set 0) and **PM6** (including the replacement) samples for the systems (a) $H^+E_5\text{-Ar}$, (b) $H^+T_1E_4\text{-Ar}$, (c) $H^+T_2E_3\text{-Ar}$, (d) $H^+T_3E_2\text{-Ar}$, (e) $H^+T_4E_1\text{-Ar}$, and (f) $H^+T_5\text{-Ar}$. The number of samples is listed in legend. The intersection between two data sets (i.e., similarity ≥ 0.99) was removed (no intersection in **NNP0** vs. **PM6**). Although we tested only a few **NNP0** minima, it presents a more robust minimum search as more low-energy and new global minimum structures were found.

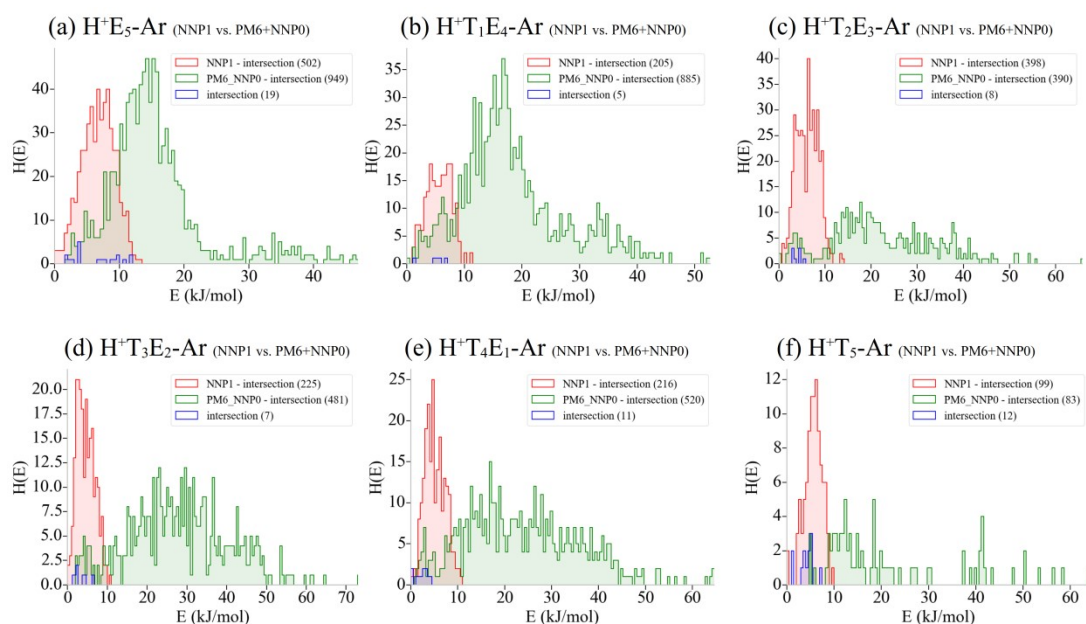


Figure S21. The histogram of zero-point corrected energies for NNP1 and PM6+NNP0 samples. We compared the locally optimized energies at the M06-2X+D3 level from NNP1 (test set 1) and PM6+NNP0 samples for the systems (a) $H^+E_5\text{-Ar}$, (b) $H^+T_1E_4\text{-Ar}$, (c) $H^+T_2E_3\text{-Ar}$, (d) $H^+T_3E_2\text{-Ar}$, (e) $H^+T_4E_1\text{-Ar}$, and (f) $H^+T_5\text{-Ar}$. The number of samples is listed in legend. The intersection between two data sets (i.e., similarity ≥ 0.99) was isolated in blue. More low-energy isomers were presented in NNP1 samples. New global minima were found in $H^+E_5\text{-Ar}$ and $H^+T_3E_2\text{-Ar}$.

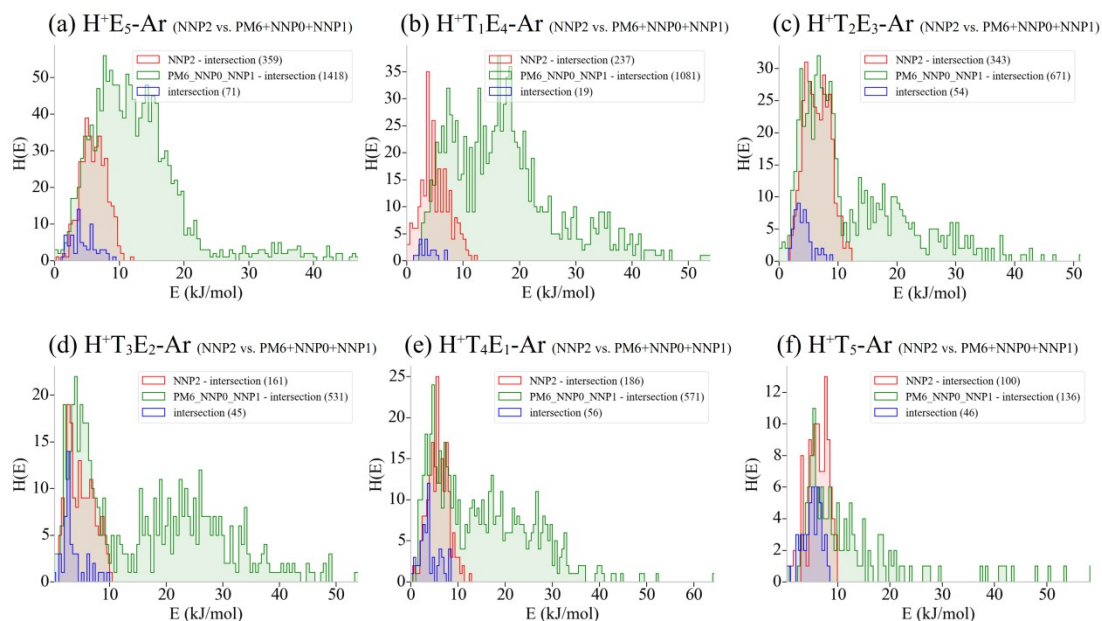


Figure S22. The histogram of zero-point corrected energies for **NNP2** and **PM6+NNP0+NNP1** samples. We compared the locally optimized energies at the M06-2X+D3 level from **NNP2** (test set 2) and **PM6+NNP0+NNP1** samples for the systems (a) $H^+E_5\text{-Ar}$, (b) $H^+T_1E_4\text{-Ar}$, (c) $H^+T_2E_3\text{-Ar}$, (d) $H^+T_3E_2\text{-Ar}$, (e) $H^+T_4E_1\text{-Ar}$, and (f) $H^+T_5\text{-Ar}$. The number of samples is listed in legend. The intersection between two data sets (i.e., similarity ≥ 0.99) was isolated in blue. More low-energy isomers were presented in **NNP2** samples. New global minima were found in $H^+T_1E_4\text{-Ar}$.

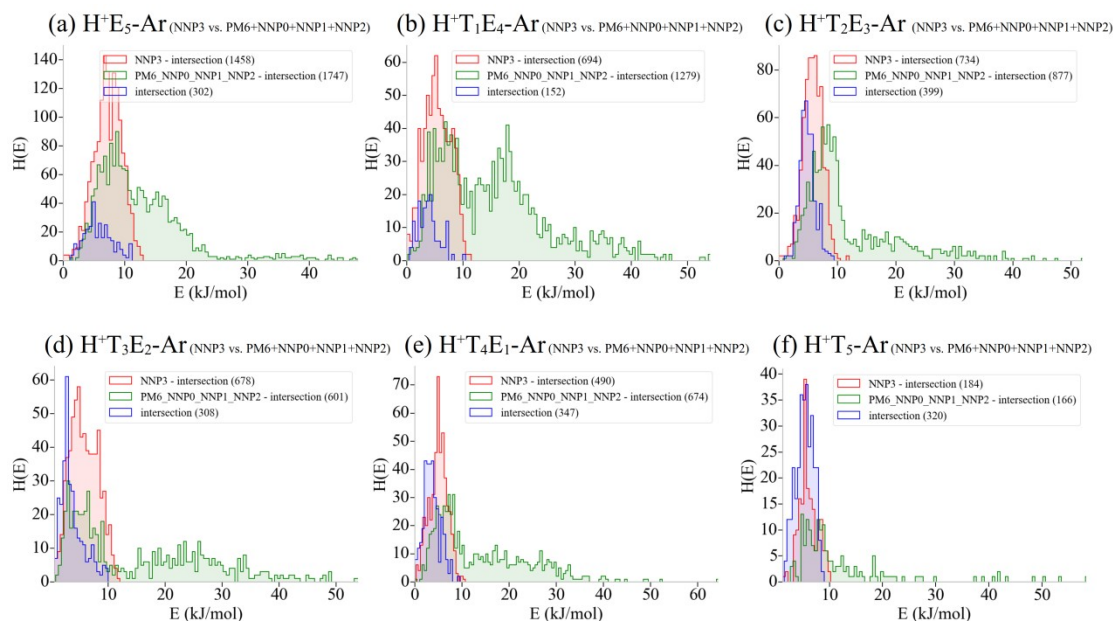


Figure S23. The histogram of zero-point corrected energies for **NNP3** and **PM6+NNP0+NNP1+NNP2** samples. We compared the locally optimized energies at the M06-2X+D3 level from **NNP3** (test set 3) and **PM6+NNP0+NNP1+NNP2** samples for the systems (a) $H^+E_5\text{-Ar}$, (b) $H^+T_1E_4\text{-Ar}$, (c) $H^+T_2E_3\text{-Ar}$, (d) $H^+T_3E_2\text{-Ar}$, (e) $H^+T_4E_1\text{-Ar}$, and (f) $H^+T_5\text{-Ar}$. The number of samples is listed in legend. The intersection between two data sets (i.e., similarity ≥ 0.99) was isolated in blue. More low-energy isomers were presented in **NNP3** samples. New global minima were found in $H^+E_5\text{-Ar}$ and $H^+T_2E_3\text{-Ar}$.

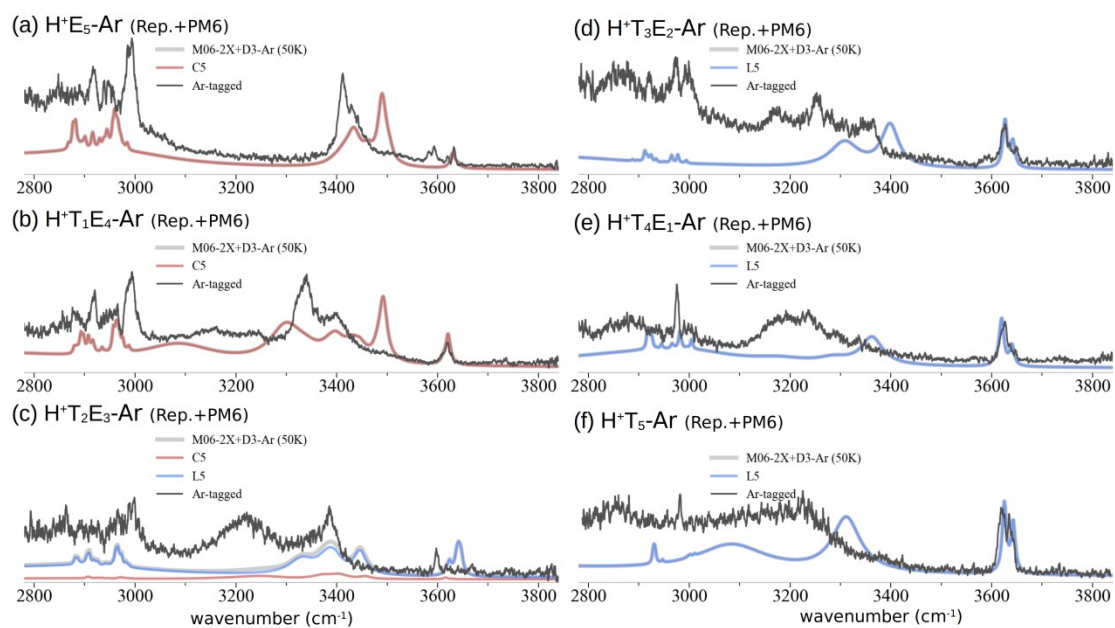


Figure S24. Comparison between the experimental and simulated IR spectra from the **PM6** and replacement samples. The simulated ones were evaluated at M06-2X+D3 level and 50K for the systems (a) $\text{H}^+\text{E}_5\text{-Ar}$, (b) $\text{H}^+\text{T}_1\text{E}_4\text{-Ar}$, (c) $\text{H}^+\text{T}_2\text{E}_3\text{-Ar}$, (d) $\text{H}^+\text{T}_3\text{E}_2\text{-Ar}$, (e) $\text{H}^+\text{T}_4\text{E}_1\text{-Ar}$, and (f) $\text{H}^+\text{T}_5\text{-Ar}$. When only a C-type or L-type structure is present, the grey curve, which represents the combined simulated spectrum of both types, will be completely covered by the corresponding colored curve for that structure.

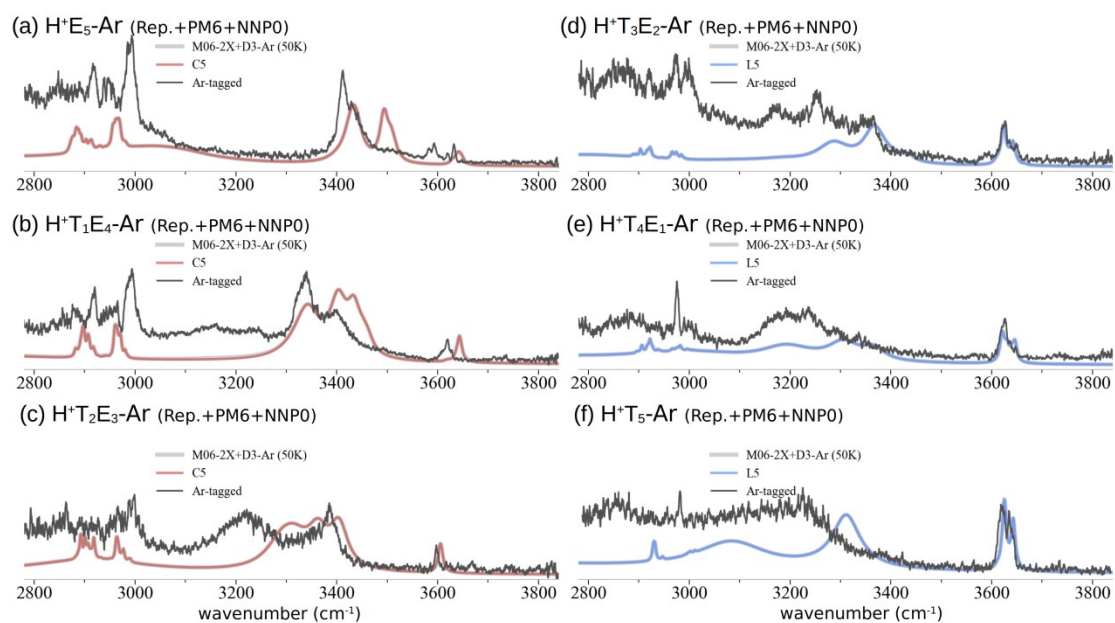


Figure S25. Comparison between the experimental and simulated IR spectra from **NNP0**, **PM6**, and replacement samples. The simulated ones were evaluated at M06-2X+D3 level and 50K for the systems (a) $\text{H}^+\text{E}_5\text{-Ar}$, (b) $\text{H}^+\text{T}_1\text{E}_4\text{-Ar}$, (c) $\text{H}^+\text{T}_2\text{E}_3\text{-Ar}$, (d) $\text{H}^+\text{T}_3\text{E}_2\text{-Ar}$, (e) $\text{H}^+\text{T}_4\text{E}_1\text{-Ar}$, and (f) $\text{H}^+\text{T}_5\text{-Ar}$. When only a C-type or L-type structure is present, the grey curve, which represents the combined simulated spectrum of both types, will be completely covered by the corresponding colored curve for that structure.

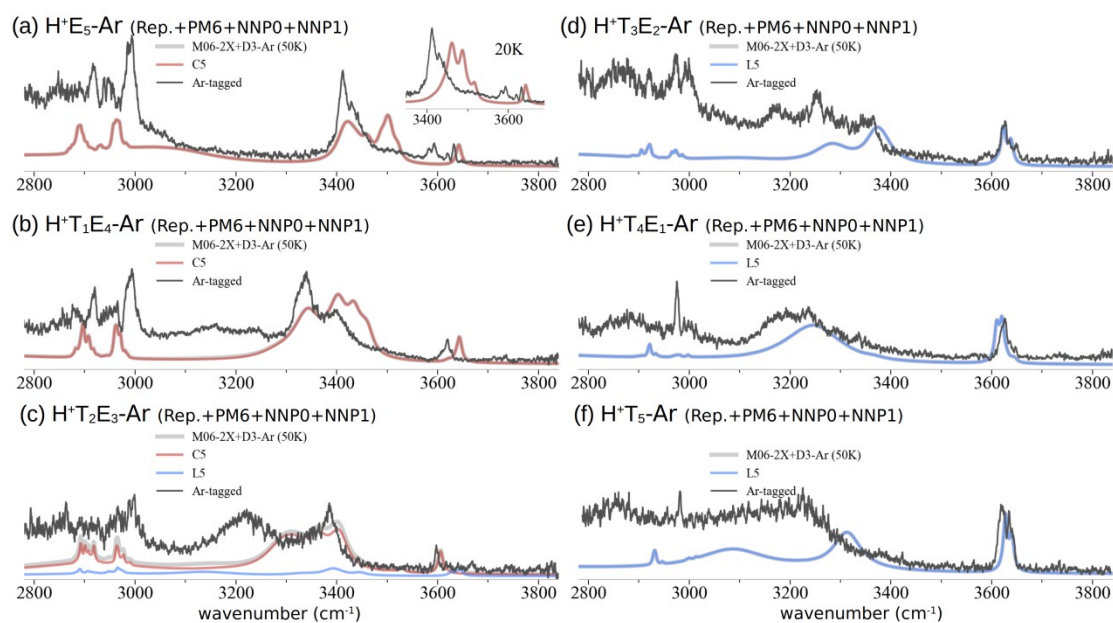


Figure S26. Comparison between the experimental and simulated IR spectra from NNP0, NNP1, PM6, and replacement samples. The simulated ones were evaluated at M06-2X+D3 level and 50K for the systems (a) $\text{H}^+\text{E}_5\text{-Ar}$, (b) $\text{H}^+\text{T}_1\text{E}_4\text{-Ar}$, (c) $\text{H}^+\text{T}_2\text{E}_3\text{-Ar}$, (d) $\text{H}^+\text{T}_3\text{E}_2\text{-Ar}$, (e) $\text{H}^+\text{T}_4\text{E}_1\text{-Ar}$, and (f) $\text{H}^+\text{T}_5\text{-Ar}$. When only a C-type or L-type structure is present, the grey curve, which represents the combined simulated spectrum of both types, will be completely covered by the corresponding colored curve for that structure.

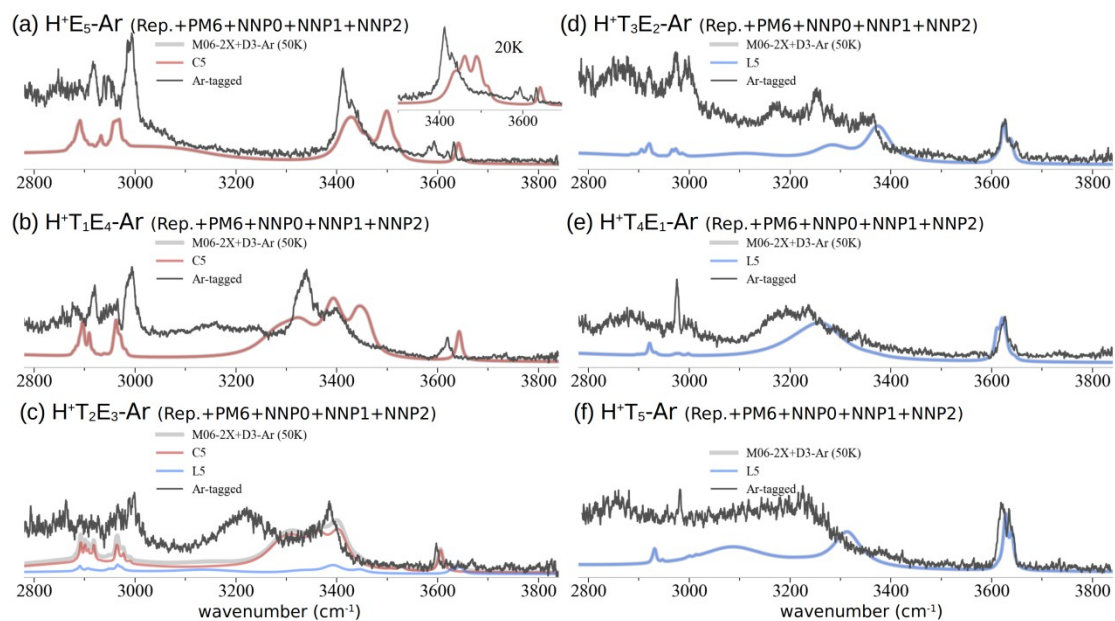


Figure S27. Comparison between the experimental and simulated IR spectra from NNP0, NNP1, NNP2, PM6, and replacement samples. The simulated ones were evaluated at M06-2X+D3 level and 50K for the systems (a) $\text{H}^+\text{E}_5\text{-Ar}$, (b) $\text{H}^+\text{T}_1\text{E}_4\text{-Ar}$, (c) $\text{H}^+\text{T}_2\text{E}_3\text{-Ar}$, (d) $\text{H}^+\text{T}_3\text{E}_2\text{-Ar}$, (e) $\text{H}^+\text{T}_4\text{E}_1\text{-Ar}$, and (f) $\text{H}^+\text{T}_5\text{-Ar}$. When only a C-type or L-type structure is present, the grey curve, which represents the combined simulated spectrum of both types, will be completely covered by the corresponding colored curve for that structure.

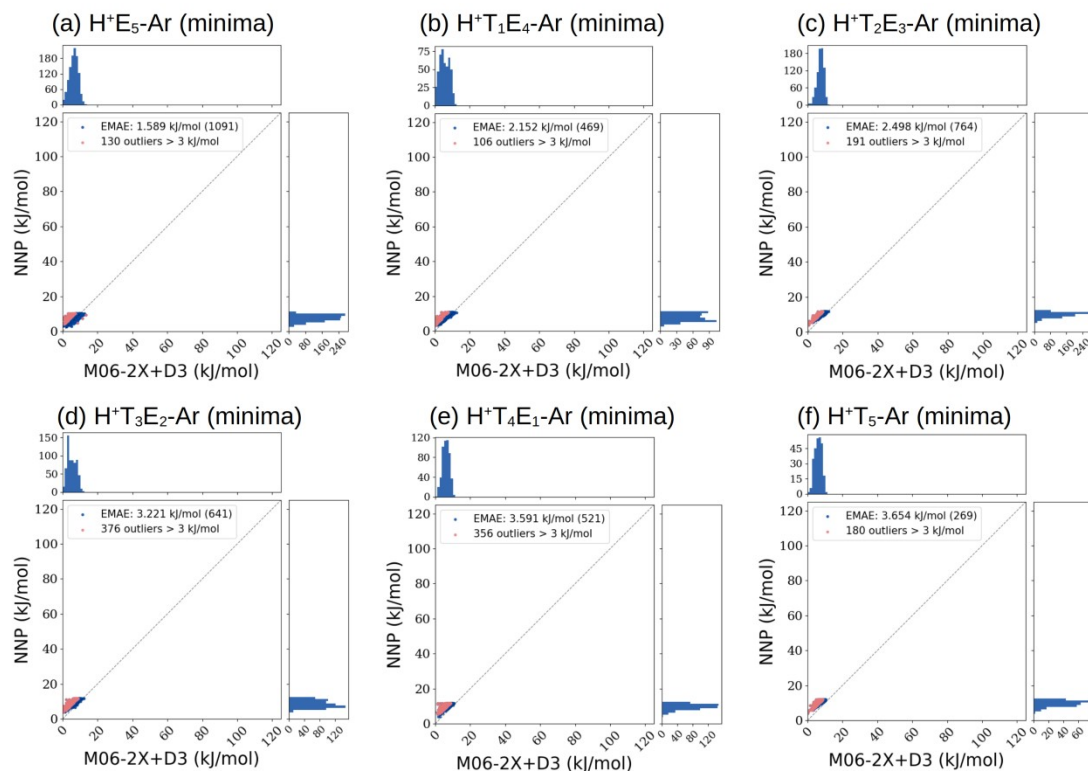


Figure S28. Energy correlation and the mean absolute error (MAE) between test set 3 from **NNP3** minima and their geometry optimization at M06-2X+D3 level using the global minimum of latter as zero energy for the systems (a) $\text{H}^+\text{E}_5\text{-Ar}$, (b) $\text{H}^+\text{T}_1\text{E}_4\text{-Ar}$, (c) $\text{H}^+\text{T}_2\text{E}_3\text{-Ar}$, (d) $\text{H}^+\text{T}_3\text{E}_2\text{-Ar}$, (e) $\text{H}^+\text{T}_4\text{E}_1\text{-Ar}$, and (f) $\text{H}^+\text{T}_5\text{-Ar}$. The M06-2X+D3 data were optimized from the **NNP3** minima within [0, 10] kJ/mol energy range. Data points with errors larger than 3 kJ/mol (outliers) are marked in red. The size of the test set and the number of outliers are listed in the legend.

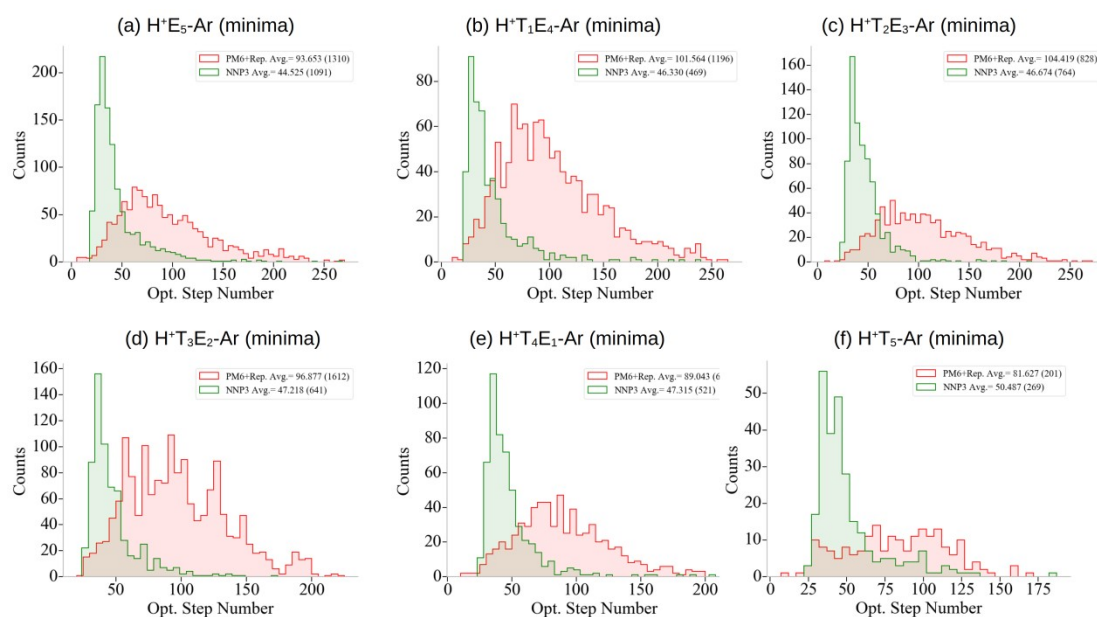


Figure S29. Comparison of optimization steps in DFT (M06-2X+D3) for the systems (a) $\text{H}^+\text{E}_5\text{-Ar}$, (b) $\text{H}^+\text{T}_1\text{E}_4\text{-Ar}$, (c) $\text{H}^+\text{T}_2\text{E}_3\text{-Ar}$, (d) $\text{H}^+\text{T}_3\text{E}_2\text{-Ar}$, (e) $\text{H}^+\text{T}_4\text{E}_1\text{-Ar}$, and (f) $\text{H}^+\text{T}_5\text{-Ar}$. The red histogram represents the number of steps required for geometry optimization based on **PM6** minima and methyl group substitution results. The green histogram shows the number of steps necessary for geometry optimization based on results from **NNP3** minima. The sample size and average number of steps are listed in the legend.

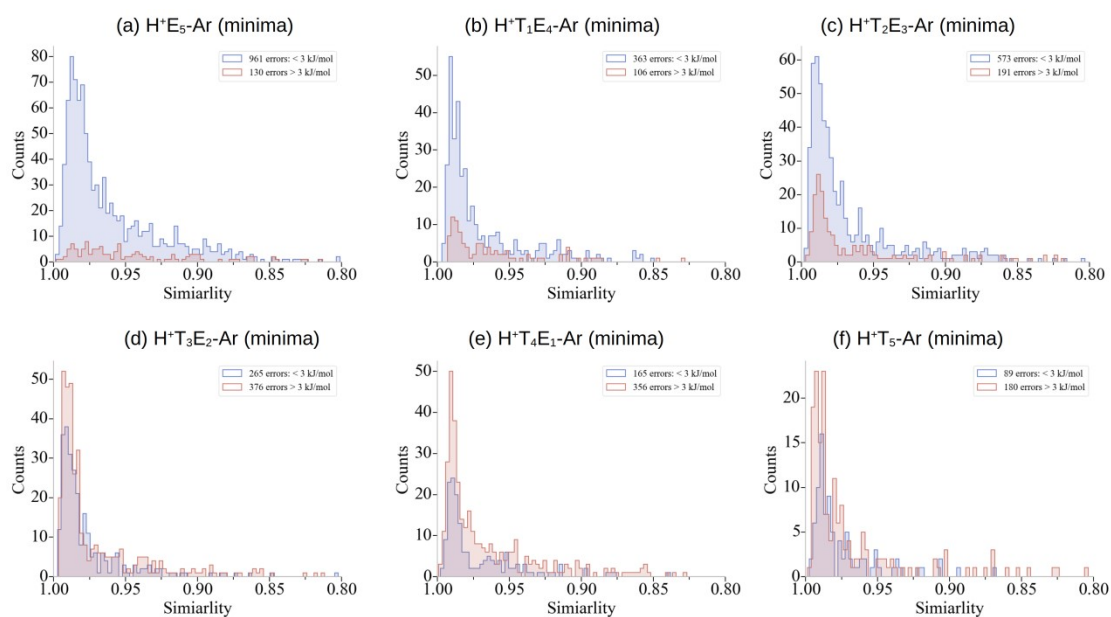


Figure S30. Statistics of shape similarity between **NNP3** minima and the corresponding DFT minima for the systems (a) $\text{H}^+\text{E}_5\text{-Ar}$, (b) $\text{H}^+\text{T}_1\text{E}_4\text{-Ar}$, (c) $\text{H}^+\text{T}_2\text{E}_3\text{-Ar}$, (d) $\text{H}^+\text{T}_3\text{E}_2\text{-Ar}$, (e) $\text{H}^+\text{T}_4\text{E}_1\text{-Ar}$, and (f) $\text{H}^+\text{T}_5\text{-Ar}$. The latter results were optimized from the former at the M06-2X+D3 level. The higher the similarity, the more similar the optimized structures of DFT and **NNP** are. We consider a similarity of 0.99 for identical structures.

References

1. T. Shinkai, P.-J. Hsu, A. Fujii, and J.-L. Kuo, *Phys. Chem. Chem. Phys.*, 2022, **24**, 12631–12644.
2. A. Fujii, N. Sugawara, P.-J. Hsu, T. Shimamori, Y.-C. Li, T. Hamashima, and J.-L. Kuo, *Phys. Chem. Chem. Phys.*, 2018, **20**, 14971-14991.
3. M. J. Frisch, G. W. Trucks, H. B. Schlegel, G. E. Scuseria, M. A. Robb, J. R. Cheeseman, G. Scalmani, V. Barone, G. A. Petersson, H. Nakatsuji, X. Li, M. Caricato, A. V. Marenich, J. Bloino, B. G. Janesko, R. Gomperts, B. Mennucci, H. P. Hratchian, J. V. Ortiz, A. F. Izmaylov, J. L. Sonnenberg, D. Williams-Young, F. Ding, F. Lipparini, F. Egidi, J. Goings, B. Peng, A. Petrone, T. Henderson, D. Ranasinghe, V. G. Zakrzewski, J. Gao, N. Rega, G. Zheng, W. Liang, M. Hada, M. Ehara, K. Toyota, R. Fukuda, J. Hasegawa, M. Ishida, T. Nakajima, Y. Honda, O. Kitao, H. Nakai, T. Vreven, K. Throssell, J. A. Montgomery, Jr., J. E. Peralta, F. Ogliaro, M. J. Bearpark, J. J. Heyd, E. N. Brothers, K. N. Kudin, V. N. Staroverov, T. A. Keith, R. Kobayashi, J. Normand, K. Raghavachari, A. P. Rendell, J. C. Burant, S. S. Iyengar, J. Tomasi, M. Cossi, J. M. Millam, M. Klene, C. Adamo, R. Cammi, J. W. Ochterski, R. L. Martin, K. Morokuma, O. Farkas, J. B. Foresman, and D. J. Fox, Gaussian, Inc., Wallingford CT, 2016.
4. M. Gaus, A. Goetz, and M. Elstner, *J. Chem. Theory Comput.*, 2013, **9**, 338–354.
5. M. Gaus, X. Lu, M. Elstner, and Q. Cui, *J. Chem. Theory Comput.*, 2014, **10**, 1518–1537.
6. X. Lu, M. Gaus, M. Elstner, and Q. Cui, *J. Phys. Chem. B*, 2015, **119**, 1062–1082.
7. M. Gaus, H. Jin, D. Demapan, A. S. Christensen, P. Goyal, M. Elstner, and Q. Cui, *J. Chem. Theory Comput.*, 2015, **11**, 332–342.
8. H. B. Schlegel, *J. Comp. Chem.*, 1982, **3**, 214-218.
9. K. T. Schütt, H. E. Saucedo, P.-J. Kindermans, A. Tkatchenko, and K.-R. Müller, *J. Chem. Phys.*, 2018, **148**, 241722.